Check for updates

How multi-length scale disorder shapes ion transport in lithium argyrodites

Bartholomew T. Payne,†[a] Mikkel Juelsholt, [ID] †[b] Miguel A. Pérez-Osorio,[c] Dominic L. R. Melvin,[ad] Gabriel J. Cuello,[e] Emmanuelle Suard, [ID] [e] Daniel J. M. Irving, [ID] [f] Nicholas H. Rees, [ID] [g] Mark Feaviour,[h] Enrico Petrucco,[h] Stephen P. Day, [ID] [h] Gregory J. Rees [ID] *[ad] and Peter G. Bruce [ID] *[adg]

The rate performance of all-solid-state batteries can be limited by the low conductivity of the solid electrolyte in the composite cathode. A conductivity of 10 mS cm^{-1} is required, which exceeds that of many solid electrolytes. This limitation can be attributed to intra- and inter-grain ion transport. Understanding the limitations of ion transport is a multi-length scale problem ranging from single bond hops to particle–particle transport. Here we show that spark plasma sintering of Li_6PS_5Cl not only enhances ion transport on the macroscopic length scale but also on the microscopic scale. On the macroscopic length scale, greater densification improves particle-to-particle contact. On the nanoscale, short-range order (SRO) of the neighbouring 4a/4a and 4d/4d Wyckoff sites present in the cold-pressed Li_6PS_5Cl produces unfavourable Li ion pathways through the cell. Spark plasma heating removes the SRO, creating a connected network of microscopic pathways for the Li to migrate. Finally, on the atomistic level, spark plasma heating increases the amount of Cl$^-$ residing on the 4d site and S^{2-} on the 4a site. By understanding the limitations of ion mobility across a range of length scales, one can target methods to produce solid-state argyrodite electrolytes with higher ionic conductivities.

Broader context

The development of better batteries is critical for decarbonisation of the transport sector. Replacing the liquid electrolyte currently used in commercial batteries with a solid electrolyte has potential to provide batteries with much higher energy densities, through the use of Li-metal anodes. However, for this to become a reality, solid state electrolytes with Li-ion conductivities exceeding 10 mS cm^{-1} are required to enable practical charge and discharge rates. Using X-ray and neutron total scattering, we have revealed the effect of short-range order (SRO) on lithium-ion transport in solid electrolytes for the first time. We demonstrate that SRO is not beneficial to ion transport in solid-state electrolytes. By removing the short-range occupational order of Cl$^-$ and S^{2-} in the anion host lattice, the conductivity can be increased significantly. These insights pave the way for manufacturers to optimise synthetic conditions to control disorder in lithium argyrodites, allowing for faster ion transport in all-solid-state batteries.

[a] *Department of Materials, University of Oxford, Oxford, UK.*
   E-mail: gregory.rees@materials.ox.ac.uk, peter.bruce@materials.ox.ac.uk
[b] *Department of Chemical Engineering, Columbia University, New York, NY 10027, USA*
[c] *SECIHTI-Dirección de Innovación y Transferencia de Conocimiento, Benemérita Universidad Autónoma de Puebla, Ciudad Universitaria, Puebla, Pue. 72570, Mexico*
[d] *The Faraday Institution, Didcot, UK*
[e] *Institut Laue-Langevin – 71 avenue des Martyrs CS 20156, 38042 Grenoble Cedex 9, France*
[f] *Diamond Light Source Ltd, Diamond House, Harwell Campus, Didcot, Oxfordshire, UK*
[g] *Department of Chemistry, University of Oxford, Oxford, UK*
[h] *Johnson Matthey Technology Centre, Blounts Ct Rd, Sonning Common, Reading, UK*

† These authors contributed equally.

Introduction

Solid-state batteries (SSBs) offer a potential route to improved energy density compared with current Li-ion batteries based on liquid electrolytes.[1–3] However, realizing high energy densities at practical rates of charge and discharge, requires solid electrolyte conductivities over 10 mS cm^{-1} to sustain sufficient ion transport within the composite cathode.[4] Such Li$^+$ conductivities have seldom been demonstrated, driving demand for the investigation of new solid electrolyte compositional spaces. Compositional exploration relies on understanding the underlying conduction mechanisms and pathways.[5–7] Sulphide solid electrolytes with the argyrodite structure, Li_6PS_5X (X = Cl, Br, I), have received significant attention due to their high ionic conductivities and soft
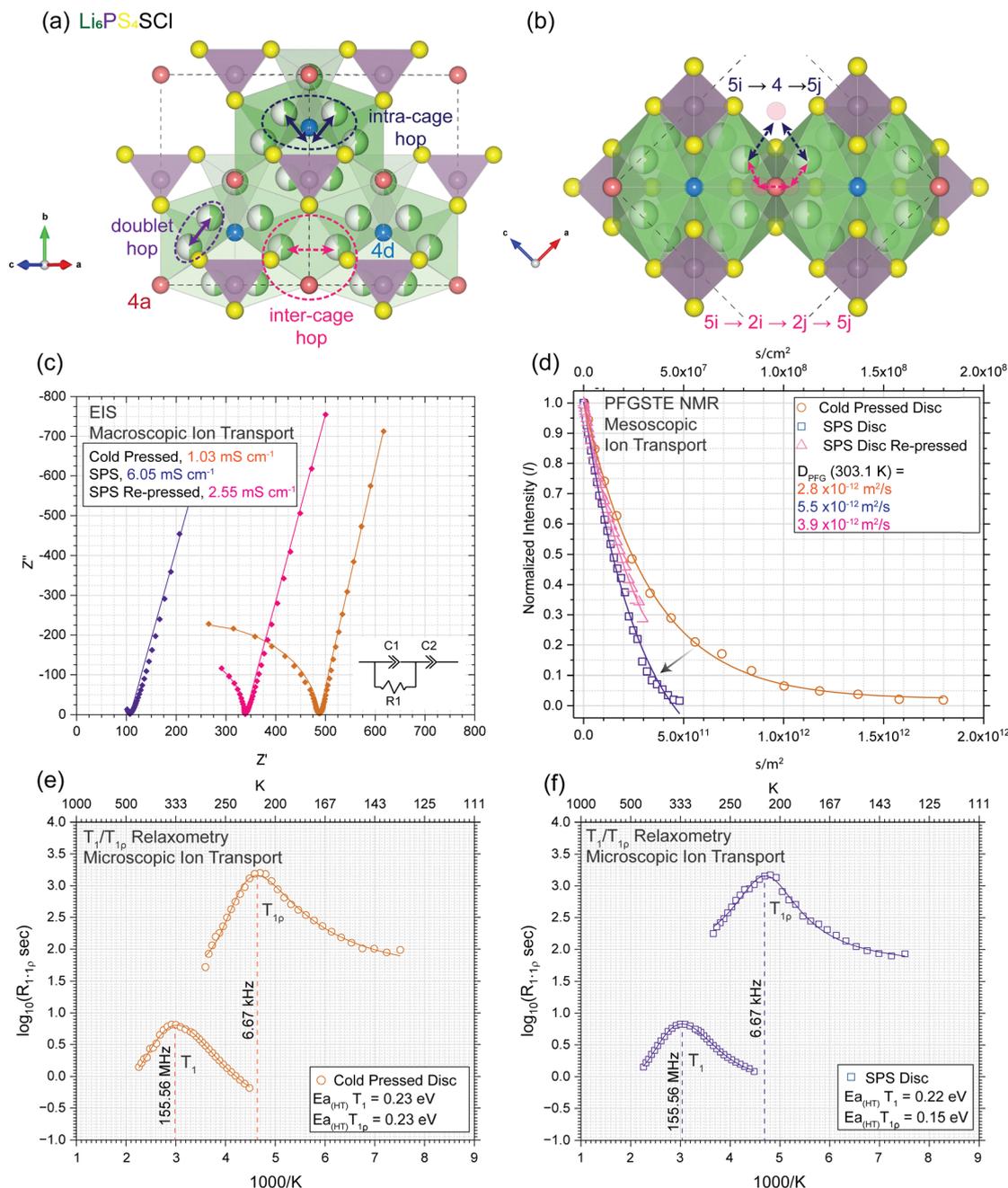
8876 | *Energy Environ. Sci.*, 2025, **18**, 8876–8888

This journal is © The Royal Society of Chemistry 2025

Fig. 1 Ion dynamics over a range of length scales. (a) The Li_6PS_5Cl structure with the 4a and 4d sites highlighted along with the primary ion transport steps. (b) The two ion transport pathways between the two cages. For clarity, four Li^+ ion tetrahedra on the underside have been removed. Li is shown in green, S in yellow, P in purple, S or Cl on a 4a site in red, and S or Cl on a 4d site in blue. (c) Electrochemical impedance spectroscopy (EIS) for cold-pressed Li_6PS_5Cl (orange, 1.03 mS cm^{-1}) and spark plasma sintered Li_6PS_5Cl (blue, 6.05 mS cm^{-1}). The SPS re-pressed (pink, 2.55 mS cm^{-1}) is a spark plasma sintered Li_6PS_5Cl that was ground up and then re-pressed in to a disc, removing any improvements due to densification. (d) Pulsed field gradient stimulated echo (PFGSTE) decay curves fitted to the Steskjal–Tanner equation at 303.1 K. (e) Cold-pressed disc and (f) SPS disc spin-lattice ($R_1 = T_1^{-1}$, $\omega_0 = 155.54$ MHz) and spin-lock ($R_{1\rho} = T_{1\rho}^{-1}$, $\omega_1 = 6.67$ kHz) relaxation over a temperature range from 123.1 to 443.1 K. The plots are fitted using the Bloembergen–Purcell–Pound (BPP) theory to give a Lorentzian peak, $J(\omega_0\tau) \propto C\dfrac{2\tau}{1 + (\omega_0\tau)^\beta}$. The lower temperature flank of the peak is typically affected by coulombic interactions and disorder. The corresponding R_1 and $R_{1\rho}$ curves for the SPS re-press are given in Fig. S3.

mechanical properties making them a good candidate for Li SSBs.[8–19] Despite their growing importance, the key bottlenecks that affect efficient Li^+ transport remain unclear.

The Li_6PS_5X structure (Fig. 1a), space group $F\bar{4}3m$, consists of a face-centred cubic arrangement of S^{2-} and X^- halide ions

(4a Wyckoff site). The central phosphorous of the PS_4^{3-} tetrahedra occupy the available octahedral sites (centred at the 4b Wyckoff site), whereas the remaining S^{2-} and X^- ions occupy half of the tetrahedral sites (4d Wyckoff site).[9] The anionic scaffold forms a network of tetrahedral cationic sites capable of

This journal is © The Royal Society of Chemistry 2025

Energy Environ. Sci., 2025, **18**, 8876–8888 | **8877**

accommodating Li$^+$. Deiseroth *et al.* introduced a 'type' formalism to differentiate between the various tetrahedra occupied by Li$^+$.[20] The lowest energy site for Li$^+$ to reside is known as a type-5 tetrahedra, defined by vertices containing the 4a and 4d sites as well as two S from different PS_4^{3-} units. Type-5 sites are the most populated Li$^+$ environments in the structure, with some studies showing half occupancy, which would account for all the Li$^+$ in the structure.[13] These type-5 tetrahedra pair up through an S–4d–S trigonal face forming a trigonal bipyramid. This face accommodates the type-5a site which forms the lowest energy hop in the Li$^+$ conduction pathway; (5 → 5a → 5), known as the doublet hop, (Fig. 1a, purple). The type 5a site is unoccupied when X = Cl$^-$, however when X = Br$^-$ or I$^-$, 20% of all Li$^+$ populate the type-5a site.[21] Six triangular bipyramids (twelve type 5 sites) form a cage around a central 4d environment. Li$^+$ can move between bipyramid units within the same cage through type-2 sites; tetrahedra with vertices defined by the 4a site, 4d at the centre of the cage, and two S, attached to the same PS_4^{3-} complex anion. This hopping pathway is referred to as the intra-cage hop (Fig. 1a, blue); (5 → 2 → 5).

The hop between cages (inter-cage hop in Fig. 1a) has been an area of much focus in the literature, as it represents the rate-limiting step for long-range Li$^+$ transport. To illustrate the proposed pathways for this inter-cage hop, we must introduce the final site of interest: type-4 tetrahedra. These are bounded by the 4a site and three S, from different PS_4^{3-} complex anions, at the vertices. There are two main inter-cage pathways between outermost type-5 sites (presented in Fig. 1b); (blue: $5^i → 4 → 5^j$) and (pink: $5^i → 2^i → 2^j → 5^j$), where i and j notify Li$^+$ moving from cage i to cage j.[22,23] Analysis of Li radial distribution functions (RDFs) shows broad peaks of sufficient small distances in the 2^i–2^j and $5^{i/j}$–4 pairs, which could facilitate ion hops. Zhao *et al.* suggested a third possible mechanism by maximum entropy analysis on neutron diffraction data which included a novel type-1x site.[24] However, experimentally, it is difficult to demonstrate *via* which pathway long-range Li$^+$ motion occurs and subtle structural changes (such as site occupation) may favour different pathways.

To improve long-range Li$^+$ transport, focus has been put on the occupancy of the 4a and 4d sites. Despite the Cl$^-$ and Br$^-$ argyrodites having high conductivities of a few mS cm^{-1}, the I$^-$ analogue is a comparatively poor conductor ($× 10^{-3}$ mS cm^{-1}), as I$^-$ exclusively occupies the 4a site.[10,25–27] As a result, 4a and 4d anion disorder is considered necessary to achieve the highest Li$^+$ transport rates the structure has to offer. Computational studies have supported this conclusion, with a wide tolerance of 50–75% Cl$^-$ occupancy on the 4d site being suggested as the optimum for inter-cage transport.[23,28] Although most experimental studies have failed to access Cl$^-$ 4d occupancy above ∼60%.[11]

Most previous studies have focused on the effects of chemical composition and crystal (average) structure on ionic conductivity in solid electrolytes, whereas local structural characterization has received less attention. Using pair distribution function analysis, Kraft *et al.* found a corresponding distance at 3.4 Å, which could not be explained by any structural motif in the average structure.[29] Schlenker *et al.* discussed the possibility of a monoclinic modulation to the crystal structure to account for this PDF feature.[30] Beyond this, the possible role of short-range order (SRO) in Li_6PS_5X, or solid electrolytes in general has not been explored in detail, despite the requirement for occupational disorder to allow fast Li$^+$ transport. Conversely, SRO has been an intense area of focus for disordered rocksalt cathodes, where SRO can lead to beneficial 0-TM channels that facilitate a percolating network in which Li$^+$ ion extraction is facile.[31]

Herein, we utilize dual densification and heat treatment (through spark plasma sintering, SPS) of Li_6PS_5Cl to manipulate both 4a/4d site occupancy and SRO without affecting the chemical composition. Hot-pressing and SPS, are well known methods for densification of ceramics, which can increase conductivity due to a reduction in grain boundary resistance.[32] In a conventional cold-pressed Li_6PS_5Cl, SRO supressed the formation of a network of pathways that enable facile Li$^+$ conduction. SPS of Li_6PS_5Cl changes the 4a/4d occupancy and removes the SRO. The result is an improvement in the interconnectivity between Li$^+$ cages, in turn boosting long-range Li$^+$ transport. The existence of SRO in Li_6PS_5Cl reveals an important structural parameter for understanding Li$^+$ migration in argyrodite-type solid electrolytes which requires consideration when designing novel solid electrolyte structures. This also highlights how preparation steps during the fabrication of solid-state batteries can and will change the atomic structure of the solid electrolyte. Therefore, researchers must take care to study the conductivity improvements across all length scales when developing novel SSBs.

Results and discussion

Ion transport in a battery is a multi-length scale problem that is affected by the atomic-, micro-, meso-, macro- and interfacial-structure of the cell. Separating these length scale phenomena allows one to find and ultimately design materials to avoid ion transport bottlenecks creating electrolytes with higher ionic conductivities. Fig. 1 deconvolutes the ion transport length scales utilizing electrochemical impedance spectroscopy (EIS, Fig. 1c, entire electrolyte), pulsed field gradient (PFG) stimulated echo (STE) nuclear magnetic resonance (PFGSTE NMR, Fig. 1d, bulk mesoscopic diffusion), spin-lattice relaxometry, and spin-lock relaxometry (T_1T and $T_{1\rho}T$, Fig. 1e and f, bulk microscopic diffusion).

The EIS shows an ×6 improvement in the conductivity of the SPS Li_6PS_5Cl argyrodite compared to the cold-pressed (CP) electrolyte (SPS; 6.05, whilst CP; 1.03 mS cm^{-1}, Table 1). The ionic conductivity value for the CP sample is in good agreement with Randrema and coworkers, who also used Ampcera Li_6PS_5Cl.[33] The SPS re-press regressed, showing a conductivity of 2.55 mS cm^{-1}, but still ×2.5 better than the original CP sample. Hand milling and re-pressing of the SPS disc removes any improvement caused by the increased density resulting in lower GB resistances (Fig. S1, density = 99% SPS, 83% SPS re-press and CP), however, the improvement in conductivity over

8878 | *Energy Environ. Sci.*, 2025, **18**, 8876–8888

This journal is © The Royal Society of Chemistry 2025

Table 1 Ion dynamics derived from different length scale measurements

	Ion transport method					
Li$_6$PS$_5$Cl electrolyte	EIS mS cm^{-1} (293.1 K)	PFG × 10^{-12} m^2 s^{-1} (303.1 K)	$T_1{}^a$ E_a eV	$T_{1\rho}{}^a$ E_a eV	DFT$_{(in-cage)}$ E_a eV	DFT$_{(cage-cage)}$ E_a eV
Cold-pressed	1.03	2.8	0.23	0.23	0.04	0.15
Spark plasma sintered	6.05	5.5	0.22	0.15	0.04	0.08
Spark plasma sintered re-press	2.55	3.9	0.22	0.17	0.04	0.08

^{a} The activation energies are derived from the high-temperature regimes. See SI2 and Fig. S3 for details.

CP suggests improvements to the macrostructure are not the sole factor for the enhancement in conductivity and a more local length scale change is also contributing to the improved conductivity. Furthermore, tortuosity factor calculations using the TauFactor program show that a 100% dense cold-pressed disc would have a maximum ionic conductivity of 1.99 mS cm^{-1} (Fig. S2).[34] Therefore, densification and grain growth alone cannot explain the sixfold increase in conductivity.

PFGSTE NMR probes diffusion on the mesoscopic (1–10 μm) length scale, incorporating grain boundary and particle-to-particle transport. PFGSTE NMR is an isotope-specific technique for directly measuring thermal diffusion coefficients and activation energies.[35] A brief explanation of the mechanism by which PFGSTE NMR determines thermal ion diffusion is given in supplementary information 1 (SI1). The PFGSTE measurements (Fig. 1d and Table 1) follow the trend of the EIS, an improved diffusion coefficient of ×2 is seen in the SPS over the cold-pressed disc (SPS; 5.5 × 10^{-12} m^2 s^{-1}, CP; 2.8 × 10^{-12} m^2 s^{-1}), with the SPS re-press electrolyte giving an ×1.4 increase (3.9 × 10^{-12} m^2 s^{-1}). The magnitude of improvement for PFGSTE NMR is reduced compared to EIS because of the different length scales probed. Conductivity, measured by EIS, is determined by pathways across the whole disc, whereas the diffusion coefficient from PFGSTE NMR is biased to the μm length scale. Therefore, the Li$^+$ motion measured by EIS encounters numerous particle–particle boundaries, whereas PFGSTE NMR encounters fewer, making the method more biased toward the bulk. Any improvement due to constriction resistances is compounded by the number of boundaries crossed by Li$^+$, therefore, EIS shows the largest improvement.

Despite this, we still see an improvement to the diffusion coefficient from PFGSTE NMR, which in turn hints that a smaller length scale process could also be responsible.

Spin-lattice (T_1) relaxation and spin-lock relaxation ($T_{1\rho}$) are routinely used to determine the activation energy for microscopic ion migration in solid-state electrolytes.[36–38] A brief generalised explanation of how relaxometry can be utilized to measure ion dynamics is given in SI2. Fig. 1e and f show the T_xT ($R_x = T_x^{-1}$) curves for the cold-pressed and SPS Li$_6$PS$_5$Cl electrolytes, respectively. The maximum for the cold-pressed appears at an appreciably higher temperature (+5–8 K) than that of the SPS and re-pressed samples (Fig. S3 shows the overlaid T_1 and $T_{1\rho}$ results that are summarized in Table 1) at both the short timescale $T_{1\rho}$ and longer timescale T_1. The high-temperature flank activation energy derived from the T_1 relaxometry measurements ($E_{a(HT)}T_1$) is similar (0.22–0.23 eV) for both the cold-pressed and SPS Li$_6$PS$_5$Cl disc. However, the activation energy from the more local $T_{1\rho}$ measurements ($E_{a(HT)}T_{1\rho}$) shows that the SPS has a reduced activation energy (0.15–0.17 eV compared to 0.23 eV for the cold-pressed). This suggests the SPS has induced an improvement in conductivity due to a change in structure on a more local length scale. To investigate these local structural changes, we employed a combination of X-ray and neutron powder diffraction and total scattering with pair distribution function analysis.

The structures of the cold-pressed and SPS samples were obtained from combined Rietveld refinement of X-ray and neutron powder diffraction (Fig. 2). Minor unreacted LiCl and Li$_2$S starting materials are observed, totalling less than 2 wt%.
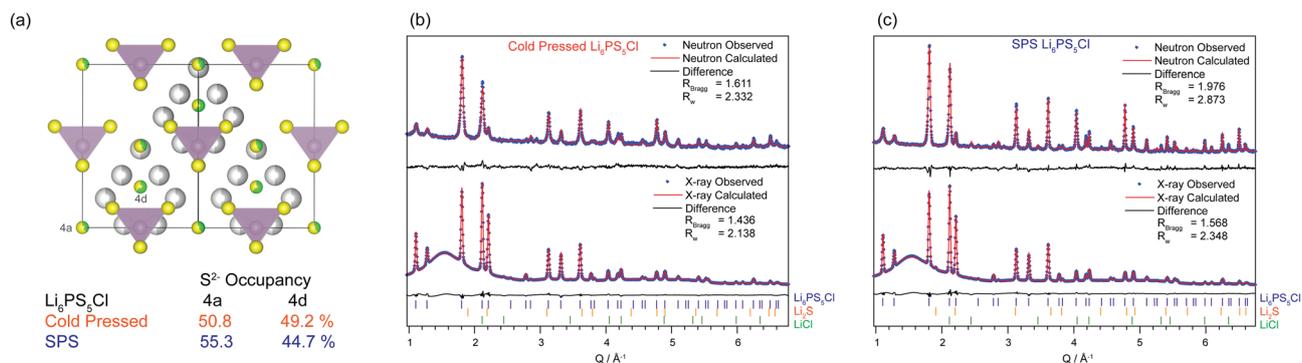

Fig. 2 Structural refinements. (a) The argyrodite Li$_6$PS$_5$Cl structure with the 4a and 4d sites labelled, their refined occupancies are given below (a complete set of parameters is given in Tables S1–S5). The observed (blue) and calculated (red) neutron and X-ray diffraction of (b) cold-pressed Li$_6$PS$_5$Cl and (c) SPS Li$_6$PS$_5$Cl. The difference between the observed and calculated is given below in black. The background observed in the XRD is from the glass capillary used as the sample holder. The quoted R_{Bragg} is for the Li$_6$PS$_5$Cl phase.

This journal is © The Royal Society of Chemistry 2025

Energy Environ. Sci., 2025, **18**, 8876–8888 | **8879**

From our refinements, the cold-pressed material from Ampcera has a near 50:50 S^{2-} to Cl^- occupation on the 4a:4d sites. For the SPS electrolyte, there is an increase in sulphur occupancy of the 4a (55%) site compared to the 4d site (45%) caused by spark plasma heating of the sample. Due to these changes in occupancy, the local mobility as probed by $T_{1\rho}T$ relaxometry (Fig. 1f) gives an appreciably lower activation energy for the Li^+ transport in the SPS disc.

To corroborate the relationship between structural occupation and improved conductivity, density functional theory (DFT) nudged elastic band (NEB) calculations were performed (Fig. 3 and Fig. S4). The aforementioned transport limiting ion hops in the argyrodite Li_6PS_5X family are between the two cages (Fig. 1b, inter-cage hop). DFT-NEB was employed to isolate the activation energy of the inter-cage pathway (Fig. 3) and intra-cage (Fig. S4) hops in the corefined structures with their varying 4a/4d occupancies. The DFT-NEB-calculated activation energies for Li_6PS_5Cl reveal that the SPS electrolyte, with 44.7/55.3% Cl occupancy on the 4a/4d Wyckoff sites, exhibits a substantially lower inter-cage activation energy (0.08 eV) for the $5i \rightarrow 4 \rightarrow 5j$ pathway compared to the cold-pressed electrolyte, which has 49.2/50.8% Cl occupancy and an activation energy of 0.15 eV. This result is in good agreement with the $T_{1\rho}$ measurements, where the SPS electrolyte (0.15 eV) has a lower activation energy than the cold-pressed Li_6PS_5Cl (0.23 eV). There is still a length scale discrepancy between the measurements, DFT is very local site-to-site hops whilst relaxometry is bulk average microscopic length scales (vide infra, DFT does not consider longer range moieties such as short-range order). Previous longer-range (300 ps) molecular dynamics simulations are in good agreement with the measured activation energy and diffusion coefficient obtained for the cold-pressed Li_6PS_5Cl.[28,39] It should be noted that the activation energy for Li^+ hopping within the cage does not improve with increasing S^{2-} 4a occupancy (Fig. S4).
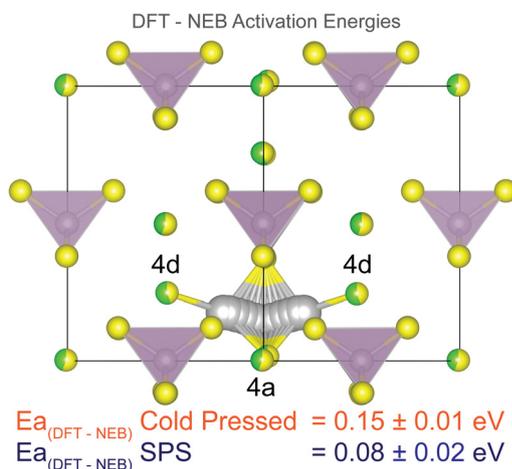

Fig. 3 Inter-cage hoping activation energies. The density functional theory (DFT) nudged elastic band (NEB) activation energies of the inter-cage hop of cold-pressed Li_6PS_5Cl and SPS Li_6PS_5Cl. The Li^+ hopping pathway is shown by the grey spheres. The intra-cage activation energies are similar for the cold-pressed and SPS electrolytes (Fig. S4). The Li transport pathway is given in grey, P in purple, S in yellow and the 4a/4d sites are in yellow (S) and green (Cl).

The Li^+ mobility, derived from the measurements in Fig. 1, improves across all length/time scales. Our previous work shows the role of the microstructure and here we have established the role of the local site occupancy in improving the conductivity.[40] Ultimately, we apply total scattering with PDF analysis to determine the local structure along the ion migration pathways.

Fig. 4b shows a comparison between the PDF calculated from the average structure obtained from the X-ray and neutron diffraction co-refinements (Fig. 2) and the experimental X-ray PDF of the cold-pressed electrolyte. Significant differences are observed at 2.5, 3.4 and 4.1 Å. The Li–Cl/S distance at 2.5 Å, predicted to be a single distance in the calculated PDF, is split into two distances in the experimental PDF (highlighted in cyan in Fig. 4b). This splitting can be accounted for by considering the Cl^-/S^{2-} occupancies on the 4a/4d sites. Sulphur at the centre of the cage (4d) causes a small cage expansion compared to a chlorine-centred cage, which results in a variation in the cage sizes. In turn, this causes the Li in the cages to have two unique interatomic distances. The three peaks between 3.4 and 4.1 Å represent the S–S distance (3.4 Å) in the PS_4^{3-} tetrahedra, the S–S distance between two neighbouring tetrahedra (3.65 Å), and the distance between the S in the PS_4^{3-} tetrahedra and 4a/4d sites (4.1 Å). The calculated PDF in Fig. 4b does not reproduce these peaks very well. Previously, this has been assigned to a local monoclinic modulation; however, we ascribe the poor description to the differences in the inter- and intramolecular correlated motion between the PS_4^{3-} tetrahedra.[30] The argyrodite material contains complex ions, PS_4^{3-}, with strong intra (neighbouring atoms within molecular anions) correlated atomic motions but weak inter (neighbouring molecular anions) correlated motion. The mismatch is caused by the known challenge of simultaneous modelling inter- and intra- molecular PDF peak widths. SI3 details how we modelled the PDFs, including the peak widths.[41,42] In brief, intramolecular peaks tend to be substantially sharper than intermolecular peaks as the intramolecular distances are dominated by the strong directional bonding from the covalent bonds, in this case, the P–S bonds. Intermolecular peaks are much less correlated which in the argyrodite is caused by the uncorrelated vibrational and rotational motion of neighbouring PS_4^{3-} units.[43]

By considering the Li–S/Cl bond splitting and the correlated motion associated with covalent bonding in PS_4^{3-} tetrahedra, the PDF fit at low r(Å) improves (Fig. 4c). However, at longer distances, 8–15 Å, the fit of the PDF is still comparatively poor. Direct comparison of the neutron PDFs for cold-pressed and SPS samples (Fig. S5) shows substantial differences in this region. The fit for the cold-pressed material can be improved by considering short-range order (SRO) between the 4a and 4d sites, i.e. the preference for ordering S and Cl on the 4a and 4d environments. The addition of SRO gives an improved X-ray and neutron PDF fit for the cold-pressed material (Fig. 4d) and is shown clearly in the calculated radial distribution functions (RDFs, i.e. the probability of finding two atoms separated by a given distance) in Fig. 4e, obtained from the fits to the PDF of cold-pressed Li_6PS_5Cl. It should be noted that Cl–S configurations are preferentially formed at a distance of ~ 7 Å,
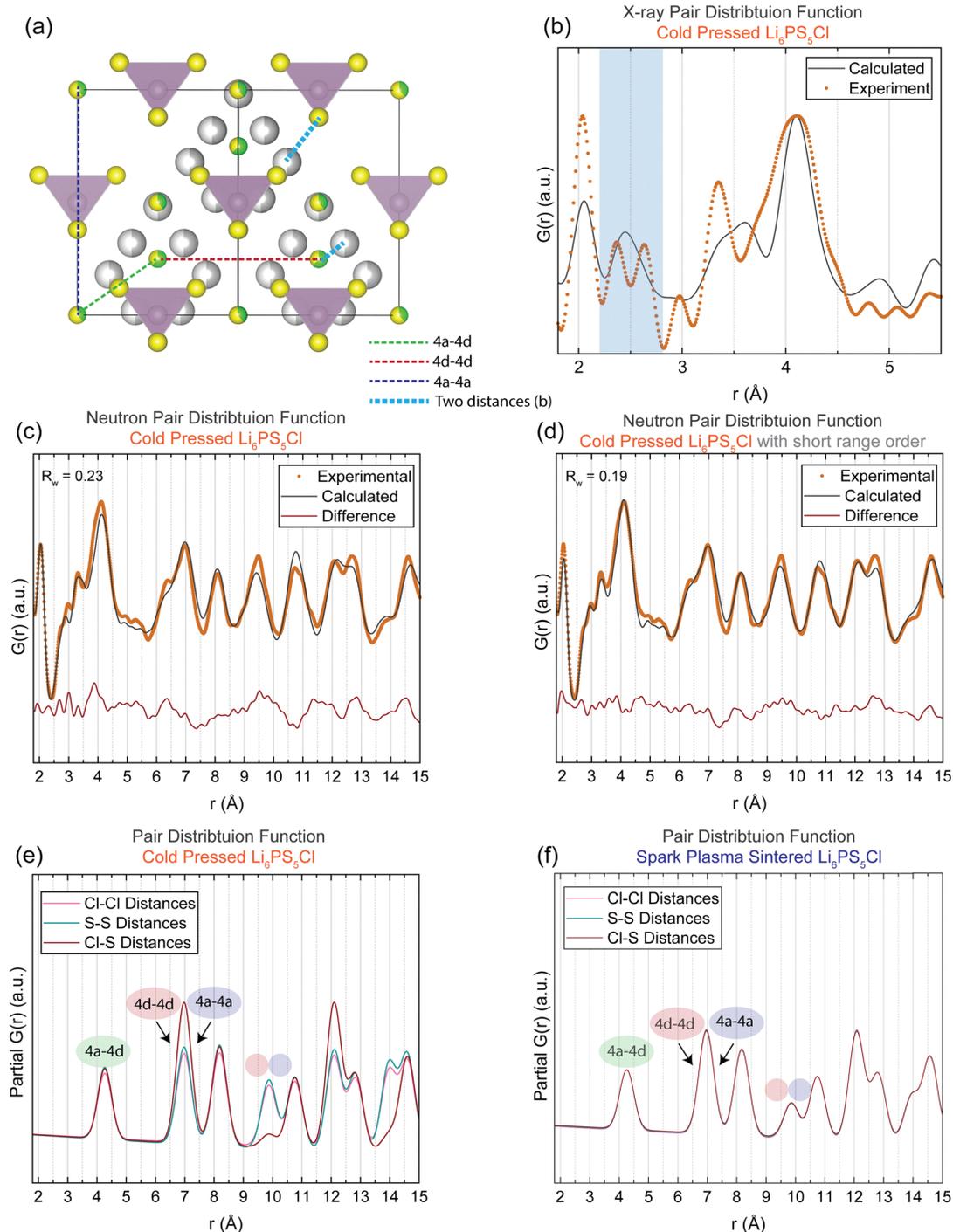
8880 | Energy Environ. Sci., 2025, 18, 8876–8888

This journal is © The Royal Society of Chemistry 2025

Fig. 4   Short-range order. (a) The structure of Li_6PS_5Cl with the 4a–4d (green), 4a–4a (blue), and 4d–4d (red) distances is given as dashed lines. Li is shown in grey, P in purple, S in yellow and Cl in green. (b) A comparison of the PDF predicted from the diffraction refinements and the experimental X-ray PDF. Two distinct Li–S/Cl distances are observed in the experimental data (highlighted in the cyan band), whilst the diffraction simulated PDF predicts a single average distance. These two distances are shown as cyan dashed lines on the structure in (a). (c) The experimental and calculated neutron PDF for the cold-pressed Li_6PS_5Cl, with (d) improvements to the fit observed with the addition of short-range order. All fits, with and without SRO, are given in Fig. S6. (e) The partial PDF for the cold-pressed Li_6PS_5Cl shows preferential 4d–4d and 4a–4a ordering compared to (f) the disordered SPS Li_6PS_5Cl, which has no SRO. The presented S–Cl/S distances are only the 4a/4d environments and do not include the PS_4 tetrahedra. The blue/red circles highlight the distance of the second 4d–4d and 4a–4a coordination sphere.

corresponding to the first-neighbour 4d–4d and 4a–4a site distances. In contrast, the second-neighbour 4d–4d and 4a–4a distances exhibit a pronounced preference for homonuclear Cl–Cl and S–S configurations. However, the model reveals no significant preference for any configurations between adjacent 4a–4d sites.

The PDF of the SPS Li_6PS_5Cl shows no improvement to the fit when SRO is considered (Fig. 4f and Fig. S6). This establishes that the SPS has very little 4a/4a or 4d/4d sulphur–chlorine SRO. Comparative refinements of the cold-pressed and SPS
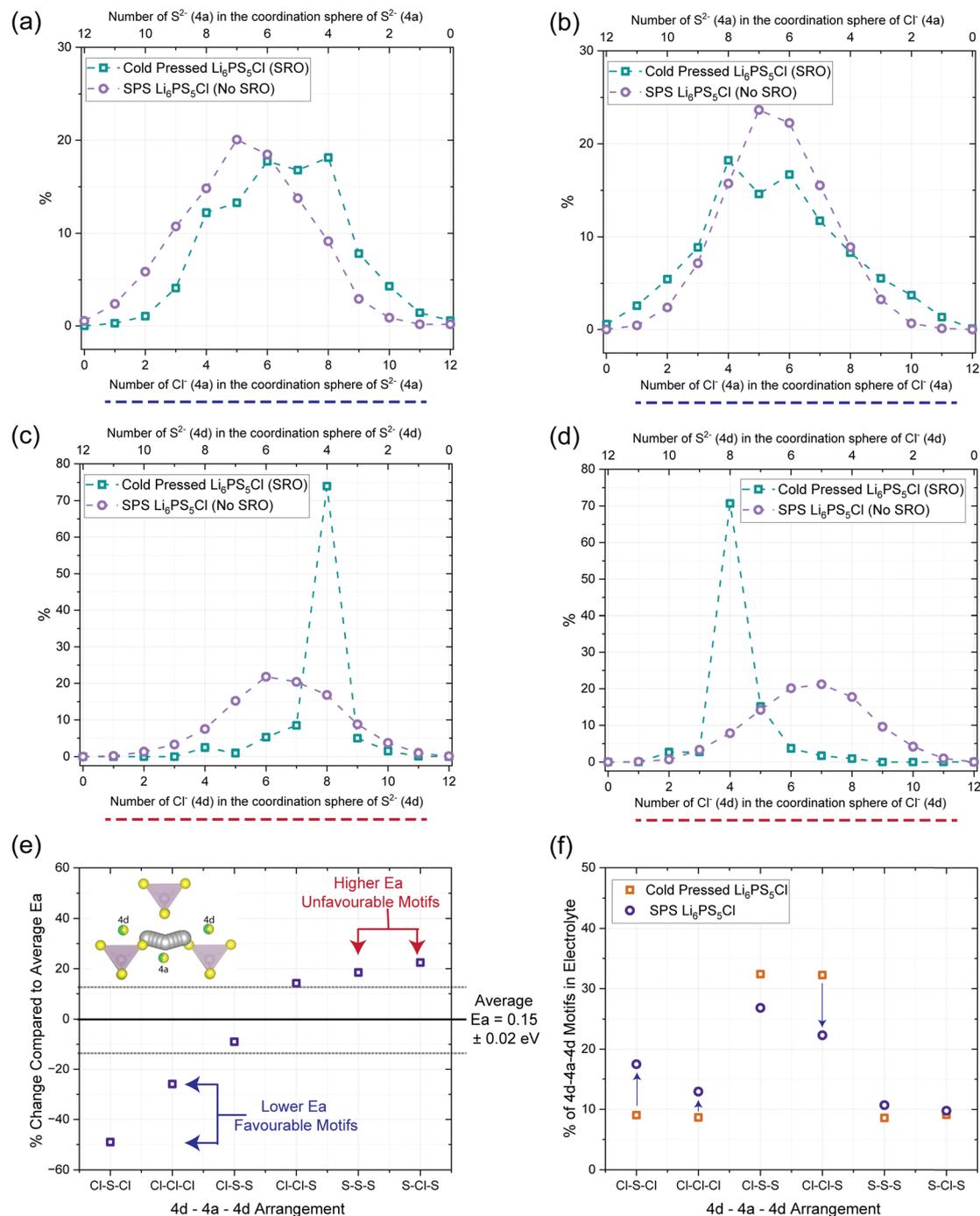

Fig. 5 The nature of the short-range order. The pair distribution function (PDF) refinements allow for statistical sampling of SRO using a supercell with 4a/4d Cl^-/S^{2-} SRO. Panels (a)–(d) illustrate the most probable neighbouring elements: (a) nearest 4a neighbour for an S^{2-} ion on a 4a site, (b) nearest 4a neighbour for a Cl^- ion on a 4a site, (c) nearest 4d neighbour for an S^{2-} ion on a 4d site, and (d) nearest 4d neighbour for a Cl^- ion on a 4d site. In the cold-pressed Li_6PS_5Cl, short-range ordering is evident, with a preference for S^{2-} occupying 4d sites that are adjacent to approximately 8 Cl^- and 4 S^{2-} anions on neighbouring 4d sites. (e) DFT-NEB-calculated activation energies for various 4d–4a–4d anion configurations. The reported values represent the average for both hopping directions (i.e., Cl–S–S and S–S–Cl). (f) The distribution (%) of 4d–4a–4d anion arrangements in the cold-pressed and SPS Li_6PS_5Cl, derived from xPDF and nPDF analyses. The SPS Li_6PS_5Cl has significantly more of the lowest activation energy pathways. A purely random distribution of arrangements would result in 12.5% for Cl–S–Cl, Cl–Cl–Cl, S–S–S and S–Cl–S and a 25% Cl–S–S/S–S–Cl and Cl–Cl–S/S–Cl–Cl for the cold pressed Li_6PS_5Cl.

8882 | Energy Environ. Sci., 2025, **18**, 8876–8888

This journal is © The Royal Society of Chemistry 2025

Li_6PS_5Cl electrolytes both with and without SRO are given in Fig. S5. The SRO will affect the likelihood for Li^+ encountering low or high energy jumps when moving between the cages around 4d sites. To explore how the SRO affects the local ion transport pathways we constructed $8 \times 8 \times 8$ supercells both with and without SRO that reproduces the partial Cl–S, Cl–Cl, and S–S PDFs obtained from the PDFgui refinement (Fig. S7). The resulting distribution of coordination environments is presented in Fig. 5.

Fig. 5 presents a statistical analysis of the local short-range order (SRO) in Li_6PS_5Cl, obtained from an $8 \times 8 \times 8$ supercell that reproduces the partial Cl–S, Cl–Cl, and S–S PDFs (Fig. S7). Panels 5a and 5b show that the 4a–4a site occupancies are similar in both the cold-pressed and SPS electrolytes, following near-normal distributions. In contrast, panels 5c and 5d illustrate the more pronounced effects of SRO on the 4d–4d environment in the cold-pressed sample, where Cl^- ions at 4d sites are most frequently surrounded by 8 S^{2-} and 4 Cl^- anions. Consequently, a Li^+ hopping from a site adjacent to $Cl^-(4d)$ has approximately a 66% probability of entering a site adjacent to $S^{2-}(4d)$. However, the SPS electrolyte displays a more randomized, near-normal distribution for 4d–4d coordination, albeit slightly off-centre due to the different average 4a/4d site occupancy.

As noted in previous studies and corroborated by the DFT-NEB results in Fig. 3, the 4d–4a–4d inter-cage ion hop is the rate-limiting step for long-range Li^+ transport. DFT-NEB calculations (Fig. 5e) reveal that two specific anion configurations, Cl–S–Cl and Cl–Cl–Cl, exhibit significantly lower activation energies (E_a) for Li^+ hops. This is consistent with the enhanced conductivity observed in the Cl-rich $Li_{5.5}PS_{4.5}Cl_{1.5}$ composition, where there is a higher probability of forming both Cl–Cl–Cl and Cl–S–Cl environments at the 4d–4a–4d motif.[44] In contrast, the S–S–S and S–Cl–S anion arrangements exhibit activation energies approximately 30% higher, explaining the intrinsically poor ionic conductivity of Li_7PS_6, which exclusively features 4d–4a–4d S–S–S motifs.[45]

Fig. 5f quantifies the distribution of favourable *versus* unfavourable 4d–4a–4d configurations in both samples. The SPS sample shows an increased proportion of the lower-E_a Cl–S–Cl and Cl–Cl–Cl motifs, resulting in a rise in the favourable lower E_a 4d–4a–4d arrangements from 50.1% (CP) to 57.2% (SPS). The number of low activation energy Cl–S–Cl arrangements is further enhanced by the concurrent increase in the S^{2-} 4a occupancy. Thus, removal of SRO creates more favourable lower activation energy inter cage pathways for Li^+ to migrate. There is no effect on the intra-cage activation energies (0.04 eV for both CP and SPS, Fig. S3) as the 4a–4d occupancies remain disordered (Fig. 4e and f).

Population sampling of different local arrangements, as above, paints an average view of Li^+ transport through Li_6PS_5Cl. The removal of SRO and the change in S^{2-} 4a occupancy will also affect the connectivity of these arrangements and this is reflected by the Haven ratio ($H_R = D_{PFG}/D_{EIS}$). Following the
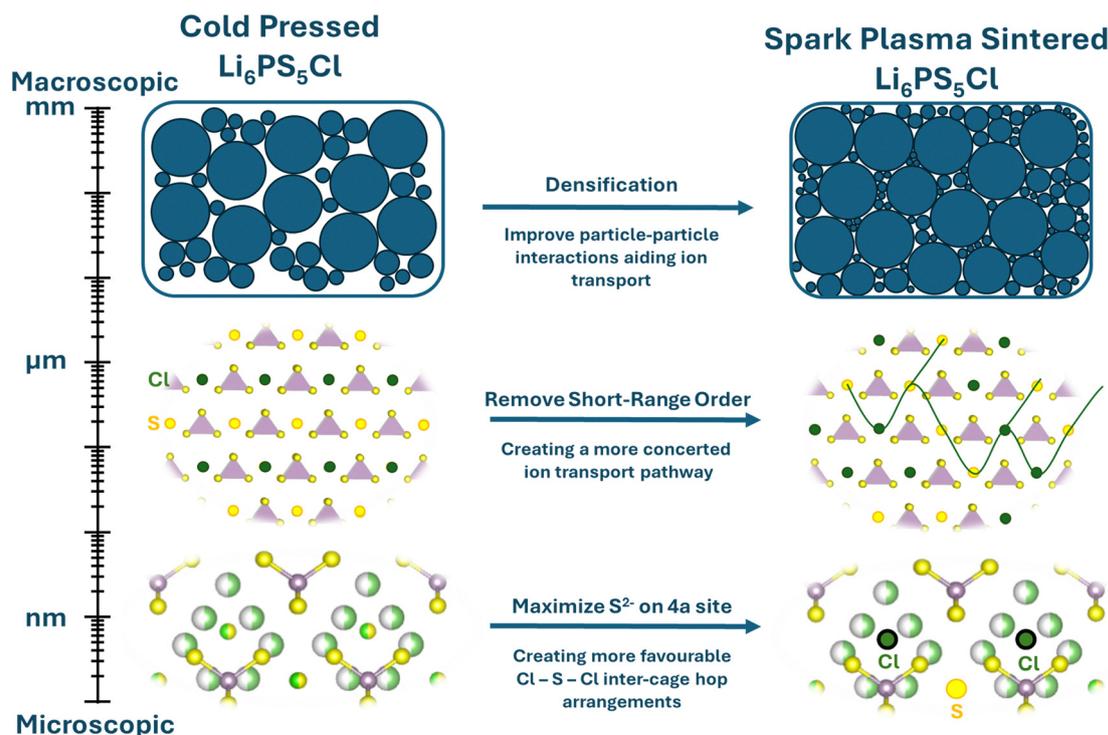

Fig. 6 Improving the conductivity of argyrodite. A schematic showing three length scale dependent parameters to target to achieve the best conductivity in Li_6PS_5Cl. On the macroscopic length scale, densification gives better particle–particle lithium-ion transport. On the microscopic length scale, the removal of short-range order and the formation of a disordered network gives a more favourable diffusion pathway. Finally, maximizing the amount of S^{2-} on the 4a site (Cl^- on the 4d site) reduces the activation energy for inter-cage lithium-ion hops by increasing the volume of the interstice.

This journal is © The Royal Society of Chemistry 2025

Energy Environ. Sci., 2025, **18**, 8876–8888 | **8883**

method outlined by Adeli and coworkers, we observe a decrease in H_R from 0.456 (cold-pressed) to 0.254 (SPS re-press), implying an increase in cage–cage connectivity, as H_R^{-1} increases from 2.2 to 3.9.[44] This enhancement in the ion transport network creates a more concerted Li^+ transport pathway due to more lower activation energy structural arrangements. Overall, the combination of removal of SRO and S^{2-} 4a occupancy contributes to the development of more effective ion transport pathways in Li_6PS_5Cl.

Conclusion

We have shown that the conductivity in stoichiometric Li_6PS_5Cl electrolytes can be improved by (illustrated in Fig. 6):

(1) Densification; this promotes a macrostructure that allows for more effective particle-to-particle lithium transport.

(2) Removal of SRO; increased local disorder in the anionic lattice forms low energy migration pathways with improved connectivity, which facilitate facile long-range Li^+ transport.

(3) Tailor occupancy on 4a and 4d sites; Li^+ transport across inter-cage pathways is enhanced when the S^{2-} occupancy on the 4a site is increased and Cl^- occupancy on the 4d site is increased.

The combination of the average and local structural changes allows for more Cl^- centred cages with enhanced inter-cage hopping rates, which are better connected *via* removal of SRO shown through a decreased Haven ratio. This in turn creates a compounded improvement to the microscopic Li-ion mobility. Our concurrent study shows that spark plasma sintering enables lithium plating at currents up to 9 mA cm^{-2} without any dendrite formation, whereas cold-pressed material shows dendritic formations at just 1 mA cm^{-2}.[40] Furthermore, loss of SRO may explain the high ionic conductivities observed in high entropy argyrodite compositions which, typically, increase the halide occupancy on 4d sites and are statistically much less likely to form SRO.[45,46]

In summary, we have shown that the diffusive processes in Li_6PS_5Cl electrolytes can be influenced across multiple length scales. The structural changes coincide with the heating regime applied during SPS; therefore, effort should be made to optimise synthesis conditions of Li_6PS_5Cl to remove short range order whilst maintaining a preference for S^{2-} on 4a and Cl^- on the 4d sites. The existence of SRO provides a new parameter to consider in the design of future solid electrolyte materials.

Experimental

Electrolyte disc formation

Ampcera Li_6PS_5Cl was purchased from MSE Supplies LLC. The electrolyte was stored and handled in an argon-filled glovebox (<1 ppm H_2O and O_2). To form the cold-pressed electrolyte discs, the argyrodite powder was densified by 400 MPa of uniaxially applied pressure at room temperature. For spark plasma sintered discs, argyrodite powder was loaded into a graphite die set which was then inserted into a spark plasma sintering system (FCT systeme GmbH) within an Ar-filled

glovebox and subject to 50 MPa uniaxial pressure at 400 °C for 5 minutes while under vacuum by passing a current through the die set. The graphite was then polished off, leaving dense discs. To form the SPS re-pressed sample, an SPS disc was hand-milled for 30 minutes and then pressed with a 400 MPa uniaxial pressure.

Impedance spectroscopy

5 mm Ni-blocking metal electrodes were sputtered onto 5 mm sample discs using physical vapour deposition (PVD). The discs were held in a 3D-printed mask before being placed in the chamber from within an argon-filled glovebox. The chamber was evacuated to a pressure of 1×10^{-5} mbar before proceeding with Ni deposition. The sputtering was repeated on the other side to create a symmetric cell with Ni-blocking electrodes.

The discs were then vacuum sealed in a pouch cell and connected to the Gamry 1010E potentiostat. Potentiostatic electrochemical impedance spectroscopy (EIS) was taken using a 5 mV voltage perturbation, collecting 10 points per decade across a frequency range of 1 MHz–0.1 Hz at 293 K, with no applied stack pressure (atmospheric pressure is sufficient to ensure current collectors contact the sputtered Ni blocking electrodes). The EIS data were analysed and fitted by equivalent circuit models using the ZView software package.

Nuclear magnetic resonance

In an argon atmosphere, 3 mm disc samples were sealed in 5 mm J-Young NMR tubes for PFG-NMR and T_1 relaxometry, whilst the same discs were sealed into 4 mm NMR rotors for $T_{1\rho}$ relaxometry. All measurements were performed under inert conditions (constant dry N_2 flow of 1500 litres per hour). The temperatures utilized (123.1 to 443.1 K) were calibrated to KBr and stabilized to 0.1 K for 240 seconds before each experiment and the relaxometry data was collected concurrently (where temperatures overlapped) with the PFGSTE experiments outlined below.[47]

Relaxometry. Spin-lattice T_1 relaxometry was determined using a saturation recovery sequence. A total of 200 saturation pulses with 250 μs separation were applied before a variable recovery delay ranging from 1 ms to 16 seconds. All data is fitted to single exponential fits using $S(t) = I_0 \left[1 - e^{\frac{-t}{T_1}} \right]$. The spin-lock $T_{1\rho}$ relaxometry experiments utilized a 6.67 kHz $B_{1\text{eff}}$ field that was varied from 1 to 180 ms. The data was fitted to $S(t) = I_0 \left[e^{\frac{-t}{T_{1\rho}}} \right]$. Both relaxometry fits had errors of <0.5%, R^2 of 0.99 with normal residual distributions.

Pulsed field gradient stimulated echoes. All pulsed field gradient (PFG) nuclear magnetic resonance (NMR) stimulated echo (STE) measurements were completed at 9.45 T ($v_0(^7Li)$ = 155.53 MHz) on Bruker Avance III HD spectrometer using a 5 mm single-axis diffusion probe with exchangeable ceramic heads. A stimulated echo pulse sequence was utilized with an effective gradient pulse duration (δ) of 1.0 ms, and a diffusion time (Δ) of 20 ms, with the gradient amplitude (g) varying between 0.1 and 24 T m^{-1} in 32 steps. All samples were sealed in a J-Young valve NMR tube, temperature stabilized to within 0.1 K, and a 4-second (T_1 = ~200 ms) recycle delay was used

8884 | *Energy Environ. Sci.*, 2025, **18**, 8876–8888

This journal is © The Royal Society of Chemistry 2025

throughout. All data is fitted to $f(x) = I_0 \times e^{-\gamma^2 g^2 \delta^2 \frac{(\Delta - \delta)}{3} D}$, where for ^{7}Li; $\delta = 1.0$ ms, $\Delta = 20$ ms, and $\gamma = 10\,397$ rad sG^{-1}. An R^2 of 0.99, errors of $<1\%$ and normal distributions of the residuals (>0.5 Shapiro Wilko score) were observed for all experiments.

Haven ratio calculations

EIS and PFGSTE-NMR data used for these calculations were both completed at 293 K (see Fig. 1c for the EIS and Fig. S8 for the 293.1 K PFGSTE NMR). The calculations were performed using the method outlined by Adeli and co-workers, which defines H_R in terms of rate-limiting steps (inter-cage hops) rather than individual ion hops.[44]

X-ray and neutron diffraction

X-ray powder diffraction was obtained from the XPDF beamline at Diamond Light Source with a wavelength of 0.1616 Å. Instrumental contributions to the peak shapes were obtained through the refinement of Si and LaB$_6$ standards. In all cases, the samples were sealed under an inert atmosphere within borosilicate capillaries. Neutron powder diffraction was measured on the high-resolution D2B instrument at Institut Laue-Langevin with a refined wavelength of 1.594983 Å.[48] The sample was packed in a sealed vanadium cylinder under argon. The Rietveld refinements were performed in Topas academic. The background was described by using a combination of a 9th-degree Chebyshev polynomial. The X-ray and neutron powder diffraction were refined in Topas Academic by simultaneously refining all structural parameters to both the X-ray and neutron datasets.[49] Each dataset had its individual background, scale factor for all phases and zero error refined. The peak shape was modelled using a Thompson–Cox–Hasting pseudo-Voigt profile. All compounds had their unit cell; symmetry allowed atomic positions and isotropic atomic displacement parameters for each atom refined. The Cl/S occupancy on the 4a and 4d sites in the argyrodite was refined but restrained such that the overall stoichiometry was kept as Li$_6$PS$_5$Cl.

X-ray and neutron pair distribution function

X-ray total scattering was obtained from the XPDF beamline at Diamond Light Source with a wavelength of 0.1616 Å. The X-ray scattering data was obtained using a PerkinElmer 4343 detector with 2880 × 2880 150 µm pixels, each 150 µm pixel size placed approximately 31 cm from the sample. In all cases, the samples were sealed under an inert atmosphere within borosilicate capillaries. The neutron total scattering experiments were conducted on the D4 two-axis diffractometer, which uses a monochromatic hot neutron beam produced at the high-flux reactor hot source at ILL (Grenoble, France).[50] The beam is diffracted by a Cu monochromator (Cu220 face) to produce a monochromatic beam of 0.5 Å wavelength, which is then collimated to achieve a beam size of 10 × 50 mm^2 (width × height) at the sample position. This position is centred with respect to the nine banks of ^{3}He detectors surrounding the sample chamber. Two Li$_6$PS$_5$Cl samples, identified as "SPS 40015" and "cold-pressed", were placed inside vanadium cylinders with an inner diameter of 6.68 mm and a wall thickness of 0.15 mm. The

packing fraction was 0.6555 and 0.5596, respectively, and both samples were fully illuminated by the neutron beam. The sample chamber was maintained at 293 K under vacuum throughout the experiment. Diffraction patterns were recorded for the samples inside the vanadium cell, the empty vanadium cell, the empty sample chamber, and a vanadium cylinder of the same dimensions as the sample. These auxiliary measurements were used for background subtraction and proper signal normalisation. As a result of these experiments, the scattered intensity was obtained as a function of the modulus of the scattering vector (Q) up to a maximum of 23.4 Å^{-1}.[51]

The PDFs were obtained using PDFgetX3 and PDFgetn3 for the X-rays and neutrons respectively.[52,53] For all samples, the scattering from an empty sample container was used as background. The model used for fitting the PDFs is further elaborated in Explanatory note 3 in the SI. The fitting was done in PDFgui2 using the Jeong peak shape model with a combination of δ_2 and σ_{ratio} to describe the correlated motion.[53] To describe the Li–S/Cl distance splitting, the Li position was split into 2 sites. For fits without SRO, the cubic unit cell, isotropic atomic displacement parameters for each atomic site, the atomic positions allowed by the $F\bar{4}3m$ space group, δ_2 and σ_{ratio} were refined. For fits with SRO the 4a and 4d sites were refined in the $P1$ space group but restrained to be between 0 and 1. The partial PDFs were calculated by PDFgui and, for ease of comparison, calculated with an U_{iso} of 0.005 Å^2 and no correlated motion.

To perform the statistical analysis of the SRO 8 × 8 × 8 supercells were generated based on a parent crystal structure using a custom Python script leveraging the pymatgen library. The atom assignment for the 4a and 4d sites was performed using a Monte Carlo scheme with a biasing mechanism: local environments were analysed using distance-based neighbour mapping, and a Boltzmann-weighted probability function favoured or disfavoured Cl–Cl/S–S or Cl–S pairs at specified distances. 7 interatomic distances were biased: the 1st 4a–4d distance, the 1st 4a–4a distance, the 1st 4d–4d distance, the 2nd 4a–4a distance, the 2nd 4d–4d distance, the 3rd 4a–4a distance and the 3rd 4d–4d distance. The 4a–4a and 4d–4d in each coordination shell had the same bias. The 8 × 8 × 8 supercells contained 2048 4d and 2048 4a sites, resulting in 24 576 of the first 4d–4d distances, 24 576 of the first 4a–4a distances, and 8192 of the first 4a–4d distances.

The combination of bias parameters for each distance that best reproduced the partial PDFs obtained from the PDFgui refinements was manually determined. The analysis of the coordination environment of the 4a and 4d site and 4d–4a–4d configurations was performed in a separate custom Python script.

Density functional theory

DFT calculations were conducted using the quantum espresso (QE) suite.[54] As exchange–correlation functional, we employed the Perdew, Burke and Ernzerhof (PBE) functional within the generalised gradient approximation (GGA).[55] The interaction between core and valence electrons was described with optimised norm-conserving Vanderbilt pseudopotentials

(ONCVSP).[56,57] The wavefunctions and charge density were represented *via* plane-wave basis sets with energy cutoffs of 120 and 480 Ry, respectively. The energy threshold was set to 1×10^{-8} eV. A $2 \times 2 \times 2$ Monkhorst–Pack k-point grids was employed. Structural models were optimised until forces on the atoms were less than 0.02 eV per Angstrom and cell stress was less than 0.5 Kbar. The compositional disorder of the 4a and 4d sites by S and Cl, in the cold-pressed and SPS Li_6PS_5Cl systems, was addressed through virtual crystal approximation (VCA), where virtual pseudopotentials containing a linearly interpolated mixed Cl and S character were prepared and used in the DFT calculations.[58] To treat the partial Li occupancy, Li ordering was investigated using combinatorics. Simple random sampling was used to choose a representative set of non-symmetry equivalent configurations for relaxation. For each system, 500 configurational models were considered. The between-cage and in-cage migration barriers of Li in Li_6PS_5Cl were computed *via* the nudged elastic band (NEB) method using the climbing image scheme as implemented in the QE suite. A total of 21 images were used to discretise the migration pathway.

Assessing the role of short-range order (SRO) by DFT or MD is challenging as long-range structural arrangements will influence the ion transport rate and percolation pathway. To simplify the problem, the activation energies of a single Li hop from a type 5_i site to neighbouring type 5_j, in the neighbouring cage was calculated, accounting for all possible permutations of anions on the 4a and 4d (S^{2-} or Cl^-) sites along the ion transport pathway. To reduce the substantial computational cost, we used unit cells containing a single Li. A jellium background was used to charge compensate the missing Li.[39] To determine the effect of Li–Li electrostatic interactions, we calculated the activation energy for one Li hop along the same path, where the 4a/4d occupancy was 49:51 and normalized the calculated activation energy (0.64 eV) to one from the fully lithiated cold-pressed simulation (0.15 eV).

Author contributions

Bartholomew T. Payne: conceptualization, methodology, formal analysis, investigation, writing – original draft, & writing – review & editing. Mikkel Juelsholt: conceptualization, methodology, formal analysis, investigation, writing – original draft, & writing – review & editing. Miguel A. Pérez-Osorio: methodology, formal analysis, investigation, writing – original draft, & writing – review & editing. Dominic L. R. Melvin: investigation, & writing – review & editing. Gabriel J. Cuello: investigation, & writing – review & editing. Emmanuelle Suard: investigation, & writing – review & editing. Daniel J. M. Irving: investigation, & writing – review & editing. Nicholas H. Rees: methodology, resources, & writing – review & editing. Mark Feaviour: investigation, & writing – review & editing. Enrico Petrucco: methodology, & writing – review & editing. Stephen P. Day: conceptualization, writing – review & editing, & supervision. Gregory J. Rees: conceptualization, methodology, formal analysis, investigation, writing – original draft, writing – review & editing, visualization, & supervision. Peter G. Bruce: conceptualization, resources, writing – original draft, writing – review & editing, & supervision.

Conflicts of interest

There are no conflicts of interest to declare.

Data availability

Acknowledgements

References

1 A. Manthiram, X. Yu and S. Wang, *Nat. Rev. Mater.*, 2017, **2**, 1–16.

2 C. Wang, J. T. Kim, C. Wang and X. Sun, *Adv. Mater.*, 2023, **35**, 2209074.

3 Q. Zhao, S. Stalin, C.-Z. Zhao and L. A. Archer, *Nat. Rev. Mater.*, 2020, **5**, 229–252.

4 A. Bielefeld, D. A. Weber and J. Janek, *ACS Appl. Mater. Interfaces*, 2020, **12**, 12821–12833.

5 R. P. Rao and S. Adams, *Phys. Status Solidi A*, 2011, **208**, 1804–1807.

6 Q. Zhang, D. Cao, Y. Ma, A. Natan, P. Aurora and H. Zhu, *Adv. Mater.*, 2019, **31**, 1901131.

8886 | *Energy Environ. Sci.*, 2025, **18**, 8876–8888

This journal is © The Royal Society of Chemistry 2025

7   Y. Kato, S. Hori, T. Saito, K. Suzuki, M. Hirayama, A. Mitsui, M. Yonemura, H. Iba and R. Kanno, *Nat. Energy*, 2016, **1**, 1–7.

8   L. Zhou, A. Assoud, Q. Zhang, X. Wu and L. F. Nazar, *J. Am. Chem. Soc.*, 2019, **141**, 19002–19013.

9   H. Deiseroth, S. Kong, H. Eckert, J. Vannahme, C. Reiner, T. Zaiß and M. Schlosser, *Angew. Chem.*, 2008, **120**, 767–770.

10 M. A. Kraft, S. P. Culver, M. Calderon, F. Böcher, T. Krauskopf, A. Senyshyn, C. Dietrich, A. Zevalkink, J. Janek and W. G. Zeier, *J. Am. Chem. Soc.*, 2017, **139**, 10909–10918.

11 I. Hanghofer, M. Brinek, S. L. Eisbacher, B. Bitschnau, M. Volck, V. Hennige, I. Hanzu, D. Rettenwander and H. M. R. Wilkening, *Phys. Chem. Chem. Phys.*, 2019, **21**, 8489–8507.

12 P. Adeli, J. D. Bazak, A. Huq, G. R. Goward and L. F. Nazar, *Chem. Mater.*, 2021, **33**, 146–157.

13 H. Deiseroth, J. Maier, K. Weichert, V. Nickel, S. Kong and C. Reiner, *Z. Anorg. Allg. Chem.*, 2011, **637**, 1287–1294.

14 M. Brinek, C. Hiebl, K. Hogrefe, I. Hanghofer and H. M. R. Wilkening, *J. Phys. Chem. C*, 2020, **124**, 22934–22940.

15 A. Gautam, M. Sadowski, N. Prinz, H. Eickhoff, N. Minafra, M. Ghidiu, S. P. Culver, K. Albe, T. F. Fässler, M. Zobel and W. G. Zeier, *Chem. Mater.*, 2019, **31**, 10178–10185.

16 V. Epp, Ö. Gün, H.-J. Deiseroth and M. Wilkening, *J. Phys. Chem. Lett.*, 2013, **4**, 2118–2123.

17 I. Hanghofer, B. Gadermaier and H. M. R. Wilkening, *Chem. Mater.*, 2019, **31**, 4591–4597.

18 A. Gautam, M. Sadowski, M. Ghidiu, N. Minafra, A. Senyshyn, K. Albe and W. G. Zeier, *Adv. Energy Mater.*, 2021, **11**, 2003369.

19 H. Wang, C. Yu, S. Ganapathy, E. R. H. van Eck, L. van Eijck and M. Wagemaker, *J. Power Sources*, 2019, **412**, 29–36.

20 H.-J. Deiseroth, J. Maier, K. Weichert, V. Nickel, S.-T. Kong and C. Reiner, *Z. Anorg. Allg. Chem.*, 2011, **637**, 1287–1294.

21 N. Minafra, M. A. Kraft, T. Bernges, C. Li, R. Schlem, B. J. Morgan and W. G. Zeier, *Inorg. Chem.*, 2020, **59**, 11009–11019.

22 J. Ding, M. K. Gupta, C. Rosenbach, H.-M. Lin, N. C. Osti, D. L. Abernathy, W. G. Zeier and O. Delaire, *Nat. Phys.*, 2025, **21**, 118–125.

23 B. J. Morgan, *Chem. Mater.*, 2021, **33**, 2004–2018.

24 E. Zhao, L. He, Z. Zhang, J.-M. Doux, D. H. S. Tan, E. A. Wu, G. Deysher, Y.-T. Chen, J. Zhao, F. Wang and Y. S. Meng, *Chem. Commun.*, 2021, **57**, 10787–10790.

25 A. Gautam, H. Al-Kutubi, T. Famprikis, S. Ganapathy and M. Wagemaker, *Chem. Mater.*, 2023, **35**, 8081–8091.

26 N. Adelstein and B. C. Wood, *Chem. Mater.*, 2016, **28**, 7218–7231.

27 P. R. Rayavarapu, N. Sharma, V. K. Peterson and S. Adams, *J. Solid State Electrochem.*, 2012, **16**, 1807–1813.

28 T. Jeon, G. H. Cha and S. C. Jung, *J. Mater. Chem. A*, 2024, **12**, 993–1002.

29 M. A. Kraft, S. Ohno, T. Zinkevich, R. Koerver, S. P. Culver, T. Fuchs, A. Senyshyn, S. Indris, B. J. Morgan and W. G. Zeier, *J. Am. Chem. Soc.*, 2018, **140**, 16330–16339.

30 R. Schlenker, A.-L. Hansen, A. Senyshyn, T. Zinkevich, M. Knapp, T. Hupfer, H. Ehrenberg and S. Indris, *Chem. Mater.*, 2020, **32**, 8420–8430.

31 J. Lee, A. Urban, X. Li, D. Su, G. Hautier and G. Ceder, *Science*, 2014, **343**, 519–522.

32 Y. Wang, R. Lim, K. Larson, A. Knab, D. Fontecha, S. Caverly, J. Song, C. Park, P. Albertus, G. W. Rubloff, S. B. Lee and A. C. Kozen, *ChemSusChem*, 2024, **17**, e202400718.

33 X. Randrema, C. Barcha, M. Chakir, V. Viallet and M. Morcrette, *Solid State Sci.*, 2021, **118**, 106681.

34 S. J. Cooper, A. Bertei, P. R. Shearing, J. A. Kilner and N. P. Brandon, *SoftwareX*, 2016, **5**, 203–210.

35 E. O. Stejskal and J. E. Tanner, *J. Chem. Phys.*, 1965, **42**, 288–292.

36 M. Wilkening and P. Heitjans, *ChemPhysChem*, 2012, **13**, 53–65.

37 A. Kuhn, M. Kunze, P. Sreeraj, H.-D. Wiemhöfer, V. Thangadurai, M. Wilkening and P. Heitjans, *Solid State Nucl. Magn. Reson.*, 2012, **42**, 2–8.

38 I. Hanghofer, B. Gadermaier and H. M. R. Wilkening, *Chem. Mater.*, 2019, **31**, 4591–4597.

39 J. Chen, M. Fang, Q. Wu, S. Tang, J. Zheng, C. Wei, X. Cao, Y. Shi, N. Xu and Y. He, *Chem. Mater.*, 2025, **37**, 591–599.

40 D. L. R. Melvin, M. Siniscalchi, D. Spencer-Jolly, B. Hu, Z. Ning, S. Zhang, J. Bu, S. Marathe, G. J. Rees, P. S. Grant, T. J. Marrow, G. Li and P. G. Bruce, *ChemRxiv*, 2024, preprint, DOI: **10.26434/chemrxiv-2024-64djb**.

41 D. Prill, P. Juhás, M. U. Schmidt and S. J. L. Billinge, *J. Appl. Crystallogr.*, 2015, **48**, 171–178.

42 N. Rademacher, L. L. Daemen, E. L. Chronister and T. Proffen, *J. Appl. Crystallogr.*, 2012, **45**, 482–488.

43 I.-K. Jeong, R. H. Heffner, M. J. Graf and S. J. L. Billinge, *Phys. Rev. B:Condens. Matter Mater. Phys.*, 2003, **67**, 104301.

44 P. Adeli, J. D. Bazak, K. H. Park, I. Kochetkov, A. Huq, G. R. Goward and L. F. Nazar, *Angew. Chem.*, 2019, **131**, 8773–8778.

45 H. Guo, J. Li, M. Burton, J. Cattermull, Y. Liang, Y. Chart, G. J. Rees, J. Aspinall and M. Pasta, *Cell Rep. Phys. Sci.*, 2024, **5**, 102228.

46 S. Li, J. Lin, M. Schaller, S. Indris, X. Zhang, T. Brezesinski, C.-W. Nan, S. Wang and F. Strauss, *Angew. Chem., Int. Ed.*, 2023, **62**, e202314155.

47 K. R. Thurber and R. Tycko, *J. Magn. Reson.*, 2009, **196**, 84–87.

48 PAYNE Bartholomew and SUARD Emmanuelle.

49 A. A. Coelho, *J. Appl. Crystallogr.*, 2018, **51**, 210–218.

50 H. E. Fischer, G. J. Cuello, P. Palleau, D. Feltin, A. C. Barnes, Y. S. Badyal and J. M. Simonson, *Appl. Phys. A: Mater. Sci. Process.*, 2002, **74**, s160–s162.

51 B. Payne and G. Cuello, *Quantifying Anion Ordering in Post-Synthesis Treatment Processes using Neutron PDF*, Institut Laue-Langevin (ILL), 2023, DOI: **10.5291/ILL-DATA.EASY-1128**.

52 P. Juhás, T. Davis, C. L. Farrow and S. J. L. Billinge, *J. Appl. Crystallogr.*, 2013, **46**, 560–566.

53 PDFfit2 and PDFgui: computer programs for studying nanostructure in crystals – IOPscience, **https://iopscience.iop.org/article/10.1088/0953-8984/19/33/335219**, (accessed 21 June 2024).

This journal is © The Royal Society of Chemistry 2025

Energy Environ. Sci., 2025, **18**, 8876–8888 | **8887**

54 P. Giannozzi, S. Baroni, N. Bonini, M. Calandra, R. Car, C. Cavazzoni, D. Ceresoli, G. L. Chiarotti, M. Cococcioni, I. Dabo, A. D. Corso, S. de Gironcoli, S. Fabris, G. Fratesi, R. Gebauer, U. Gerstmann, C. Gougoussis, A. Kokalj, M. Lazzeri, L. Martin-Samos, N. Marzari, F. Mauri, R. Mazzarello, S. Paolini, A. Pasquarello, L. Paulatto, C. Sbraccia, S. Scandolo, G. Sclauzero, A. P. Seitsonen, A. Smogunov, P. Umari and R. M. Wentzcovitch, *J. Phys.: Condens. Matter*, 2009, **21**, 395502.

55 J. P. Perdew, K. Burke and M. Ernzerhof, *Phys. Rev. Lett.*, 1996, **77**, 3865–3868.

56 M. Schlipf and F. Gygi, *Comput. Phys. Commun.*, 2015, **196**, 36–44.

57 D. R. Hamann, *Phys. Rev. B:Condens. Matter Mater. Phys.*, 2013, **88**, 085117.

58 L. Bellaiche and D. Vanderbilt, *Phys. Rev. B:Condens. Matter Mater. Phys.*, 2000, **61**, 7877–7882.

59 B. T. Payne, M. Juelsholt, M. A. Pérez-Osorio, D. L. R. Melvin, G. J. Cuello, E. Suard, D. J. M. Irving, N. H. Rees, M. Feaviour, E. Petrucco, S. P. Day, G. J. Rees and P. G. Bruce, CCDC 2430153: Experimental Crystal Structure Determination, 2025, DOI: **10.5517/ccdc.csd.cc2mks11**.

60 B. T. Payne, M. Juelsholt, M. A. Pérez-Osorio, D. L. R. Melvin, G. J. Cuello, E. Suard, D. J. M. Irving, N. H. Rees, M. Feaviour, E. Petrucco, S. P. Day, G. J. Rees and P. G. Bruce, CCDC 2430154: Experimental Crystal Structure Determination, 2025, DOI: **10.5517/ccdc.csd. cc2mks22**.